Troja, E, Sakamoto, T, Cenko, SB, Lien, A, Gehrels, N, Castro-Tirado, AJ, Ricci, R, Capone, J, Toy, V, Kutyrev, A, Kawai, N, Cucchiara, A, Fruchter, A, Gorosabel, J, Jeong, S, Levan, A, Perley, DA, Sanchez-Ramirez, R, Tanvir, N and Veilleux, S

An Achromatic Break in the Afterglow of the Short GRB 140903A: Evidence for a Narrow Jet

The Astrophysical Journal, 827:102 (12pp), 2016 August 20 doi:10.3847/0004-637X/827/2/102

AN ACHROMATIC BREAK IN THE AFTERGLOW OF THE SHORT GRB 140903A: EVIDENCE FOR A NARROW JET

E. Troja[1,2], T. Sakamoto[3], S. B. Cenko[2,4], A. Lien[2,5], N. Gehrels[2], A. J. Castro-Tirado[6,7], R. Ricci[8], J. Capone[1], V. Toy[1], A. Kutyrev[1,2], N. Kawai[9], A. Cucchiara[2,10], A. Fruchter[10], J. Gorosabel[11,12,13,18], S. Jeong[6,14], A. Levan[15], D. Perley[16], R. Sanchez-Ramirez[6], N. Tanvir[17], and S. Veilleux[1]

[1] Department of Astronomy, University of Maryland, College Park, MD 20742, USA
[2] NASA, Goddard Space Flight Center, 8800 Greenbelt Road, Greenbelt, Greenbelt, MD 20771, USA
[3] Department of Physics and Mathematics, College of Science and Engineering, Aoyama Gakuin University, 5-10-1 Fuchinobe, Chuo-ku, Sagamihara-shi, Kanagawa 252-5258, Japan
[4] Joint Space-Science Institute, University of Maryland, College Park, MD 20742, USA
[5] Department of Physics, University of Maryland, Baltimore County, Baltimore, MD 21250, USA
[6] Instituto de Astrofísica de Andalucía (IAA-CSIC), P.O. Box 03004, E-18008 Granada, Spain
[7] Unidad Asociada Departamento de Ingeniería y Sistemas Automáticos, E.T.S. Ingeniería Industrial, Universidad de Málaga, Campus de Teatinos, Arquitecto Francisco Penalosa, 6, E-29010, Málaga, Spain
[8] INAF-Istituto di Radioastronomia, Via Gobetti 101, I-40129 Bologna, 0000-0003-4631-1528, Italy
[9] Department of Physics, Tokyo Institute of Technology, 2-12-1 (H-29) Ookayama, Meguro-ku, Tokyo 152-8551, Japan
[10] Space Telescope Science Institute, 3700 San Martin Drive, Baltimore, MD 21218, USA
[11] Unidad Asociada Grupo Ciencias Planetarias (UPV/EHU, IAA-CSIC), Departamento de Física Aplicada I, E.T.S. Ingeniería, Universidad del Pas Vasco (UPV/EHU), Alameda de Urquijo s/n, E-48013 Bilbao, Spain
[12] Ikerbasque, Basque Foundation for Science, Alameda de Urquijo 36-5, E-48008 Bilbao, Spain
[13] Universidad del País Vasco, Bilbao, Spain
[14] Sungkyunkwan University, 25-2 Sungkyunkwan-ro, Jongno-gu, 1398 Seoul, Korea
[15] Department of Physics, University of Warwick, Coventry, CV4 7AL, UK
[16] Dark Cosmology Centre, Niels Bohr Institute, University of Copenhagen Juliane Maries Vej 30, DK-2100 Copenhagen, Denmark
[17] Department of Physics and Astronomy, University of Leicester, Leicester, LE1 7RH, UK
Received 2016 March 3; revised 2016 June 6; accepted 2016 June 8; published 2016 August 11

ABSTRACT

We report the results of our observing campaign on GRB 140903A, a nearby ($z = 0.351$) short-duration ($T_{90} \sim 0.3$ s) gamma-ray burst discovered by *Swift*. We monitored the X-ray afterglow with *Chandra* up to 15 days after the burst and detected a steeper decay of the X-ray flux after $t_j \approx 1$ day. Continued monitoring at optical and radio wavelengths showed a similar decay in flux at nearly the same time, and we interpret it as evidence of a narrowly collimated jet. By using the standard fireball model to describe the afterglow evolution, we derive a jet opening angle $\theta_j \approx 5^\circ$ and a collimation-corrected total energy release $E \approx 2 \times 10^{50}$ erg. We further discuss the nature of the GRB progenitor system. Three main lines disfavor a massive star progenitor: the properties of the prompt gamma-ray emission, the age and low star formation rate of the host galaxy, and the lack of a bright supernova. We conclude that this event likely originated from a compact binary merger.

Key words: gamma-ray burst: individual (GRB 140903A) – X-rays: bursts

1. INTRODUCTION

Gamma-ray bursts (GRBs) are produced by a highly relativistic outflow collimated into jets. The angular size of the outflow is therefore a key ingredient in determining the true energy release and the event rate. These parameters provide a crucial test for any progenitor and central engine model.

Measuring the collimation of short-duration GRBs, i.e., those lasting less than 2 s (Kouveliotou et al. 1993), not only is a primary interest of the GRB field but has a broader impact. Growing observational evidence connects short GRBs with compact binary mergers (Gehrels et al. 2005; Tanvir et al. 2013; Berger 2014; Yang et al. 2015, and references therein), which are among the most promising sources of gravitational wave (GW) radiation (Thorne 1987, pp. 330–458; Abbott et al. 2016b). Therefore, the degree of collimation of short GRBs is a critical input for inferring the true rate of binary mergers, the expected detection rate of advanced LIGO and Virgo (Abadie et al. 2010), and for estimating our chances to observe the electromagnetic counterpart of a GW source (Abbott et al. 2016a; Troja et al. 2016).

Observationally, the beamed geometry leaves a clear signature in the afterglow temporal evolution, manifesting itself as an *achromatic* light-curve break (known as "jet break"), visible on timescales of approximately days to weeks after the explosion (Rhoads 1999). At early times (hours after the explosion), the evolution of the afterglow is the same as for a spherical explosion. However, later on, the jet edges become visible, causing the observed flux to rapidly fall off (van Eerten et al. 2010; van Eerten & MacFadyen 2013). For a jet expanding into a homogeneous ambient medium such steepening takes place at a time $t_j \propto \theta_j^{8/3}$ (Sari et al. 1999; van Eerten et al. 2010), when the outflow is decelerated down to a bulk Lorentz factor $\approx \theta_j^{-1}$, where θ_j is the jet half-opening angle. The detection of a jet break in the afterglow light curve is therefore an important diagnostic tool for constraining the outflow geometry and the burst energetics.

In the case of short bursts, the faintness of their afterglows often hampers the search for jet breaks. Only a small fraction of short GRBs have been detected at optical or radio wavelengths, and often they are sampled too poorly to meaningfully constrain the afterglow temporal evolution (Kann et al. 2011; D'Avanzo et al. 2014). Nicuesa Guelbenzu et al. (2012)

[18] Deceased.

presented good evidence for an achromatic steepening in the optical/near-IR (NIR) light curve of the short GRB 090426. However, the classification of this burst is rather ambiguous (Antonelli et al. 2009; Levesque et al. 2010), and it was proposed that the event was more likely an interloper, originating from a massive star progenitor (Thöne et al. 2011; Virgili et al. 2011; Nicuesa Guelbenzu et al. 2012).

Candidate jet breaks have been identified in several X-ray afterglows of short GRBs (Burrows et al. 2006; Stratta et al. 2007; Coward et al. 2012; Fong et al. 2012; Zhang et al. 2015); however, their interpretation as jet breaks remains quite controversial. Several studies suggest that the X-ray light curves may be shaped by a persistent energy injection from the central engine (Fan & Xu 2006; Cannizzo et al. 2011; Rowlinson et al. 2013) rather than by external shock emission (Mészáros & Rees 1997). In this scenario the sharp decay of the X-ray flux is attributed to the rapid turnoff of the energy source rather than to the outflow geometry, and no collimation is needed to explain the observed light curves. Indeed, in the small sample of events with simultaneous optical and/or radio coverage (e.g., GRB 090510, De Pasquale et al. 2010; GRB 130603B, Tanvir et al. 2013) the observed temporal breaks appear to be chromatic rather than frequency independent. The jet-break interpretation, to still hold, would require an alteration of the basic jet model, such as a two-component jet (Corsi et al. 2010), evolving shock parameters (De Pasquale et al. 2010), or the presence of additional emission components (e.g., Gao et al. 2015).

In this paper, we present our multiwavelength campaign of the short GRB 140903A, which revealed an achromatic break in its afterglow light curve. Through the analysis of the broadband data, we show that the observed emission is fully consistent with the standard forward shock model and requires a narrowly collimated outflow. A previous analysis of this event, based on *Swift* observations, did not detect the presence of a jet break in the X-ray data (Fong et al. 2015). Our addition of deep, late-time *Chandra* observations is indeed critical for the jet-break detection and its characterization. We further investigate the GRB classification and the nature of its progenitor and conclude that this event is a bona fide short GRB, likely originating from a compact binary merger. The paper is organized as follows: our observations and data reduction procedures are detailed in Section 2; we present our analysis of the GRB prompt emission, its afterglow, and its host galaxy in Section 3; our results are discussed in Section 5. Throughout the paper, times refer to the *Swift* trigger time, and the phenomenology of the burst is presented in the observer's frame. We employ a standard ΛCDM cosmology with $H_0 = 67.8\,\mathrm{km\,s^{-1}\,Mpc^{-1}}$, $\Omega_M = 0.308$, and $\Omega_\Lambda = 0.692$ (Planck Collaboration et al. 2015). Unless otherwise stated, errors are given at the 68% confidence level for one interesting parameter, and upper limits are reported at the 3σ confidence level.

2. OBSERVATIONS AND DATA REDUCTION

2.1. Swift BAT and XRT

GRB 140903A triggered the *Swift* Burst Alert Telescope (BAT; Barthelmy et al. 2005) at 15:00:30 UT on 2014 September 3 (Cummings et al. 2014). The *Swift* X-ray Telescope (XRT; Burrows et al. 2005) began settled observations of the GRB field 74 s after the BAT trigger and monitored the X-ray afterglow during the following 3 days, until the source faded below the detector sensitivity threshold. The XRT data comprise 24 ks acquired in Photon Counting (PC) mode.

BAT and XRT data were processed using the *Swift* software package distributed within HEASOFT (v. 6.17). We used the latest release of the BAT and XRT Calibration Database and followed standard data reduction procedures.

2.2. Chandra

The *Chandra X-ray Observatory* performed two Target of Opportunity (ToO) observations in order (1) to precisely localize the X-ray afterglow (PI: T. Sakamoto) and (2) to characterize its late-time temporal evolution and search for a possible jet break (PI: E. Troja). Our first observation (ObsId 15873) started 3 days after the burst and observed the field for a total exposure of 19.8 ks. Our second *Chandra* observation (ObsId 15986) was performed on 2014 September 18 for a total exposure of 59.3 ks. *Chandra* data were reduced using version 4.6.1 of the CIAO software with CALDB version 4.6.3. Events from the GRB afterglow were selected using a source extraction radius of 2 pixels, and the derived count rates were corrected for vignetting effects and point-spread function (PSF) losses. The background contribution was estimated from an annular, source-free region centered on the afterglow position.

The GRB afterglow is detected at both epochs. In our first *Chandra* observation we detect 80 net source counts in the 0.5–8.0 keV energy band. We corrected the native *Chandra* astrometry by aligning our X-ray and optical images (see Section 2.3). Based on the match of five bright X-ray and optical sources, we determine a refined X-ray (J2000.0) position of $\alpha = 15^{\mathrm{h}}52^{\mathrm{m}}03\overset{\mathrm{s}}{.}273$, $\delta = +27^{\circ}36'10\overset{''}{.}83$ with an error radius of $0\overset{''}{.}4$ (90% confidence level). In our second and last *Chandra* observation only 6 counts are measured at the source position, corresponding to a detection significance >99.99% (Kraft et al. 1991).

2.3. Discovery Channel Telescope (DCT)

We initiated an observing campaign with the Large Monolithic Imager (LMI) mounted on the 4.3 m DCT in Happy Jack, AZ. Observations in the *griz* filters started on 2014 September 04 at 3.17 UT, approximately 12 hr after the *Swift* trigger, and continued to monitor the field for the next 3 weeks. Late-time images in the *r* and *i* filters were acquired on 2016 March 17 (561 days after the burst) and used as templates for image subtraction. Standard CCD reduction techniques (e.g., bias subtraction, flat-fielding, etc.) were applied using a custom IRAF[19] pipeline. Individual short (10–20 s) exposures were aligned with respect to astrometry from the Sloan Digital Sky Survey (SDSS; Ahn et al. 2014) using SCAMP (Bertin 2006) and stacked with SWarp (Bertin et al. 2002).

As shown in Figure 1, the field of GRB 140903A is quite complex: the optical afterglow lies on top of a relatively bright host galaxy (see below), and only $12''$ away from an extremely bright ($V \approx 9$ mag) star. In order to extract the afterglow brightness from our DCT images, we performed digital image subtraction with the High Order Transform of PSF ANd Template Subtraction (HOTPANTS; Becker 2015). The resulting photometry, calibrated with respect to nearby point

[19] IRAF is distributed by the National Optical Astronomy Observatory, which is operated by the Association of Universities for Research in Astronomy (AURA) under cooperative agreement with the National Science Foundation.

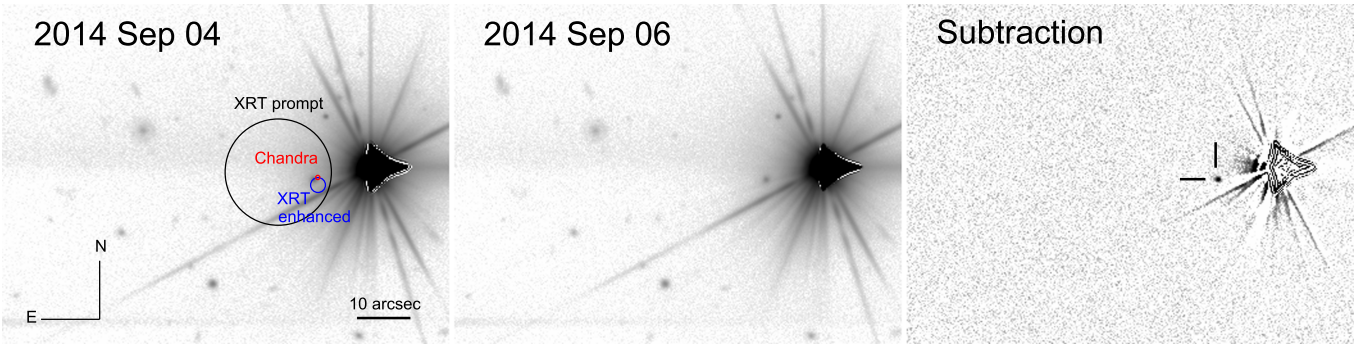

Figure 1. DCT *r*-band observations of the field of GRB 140903A, taken at 0.5 days (left panel) and 2.5 days (middle panel) after the burst. The black circle shows the initial XRT afterglow localization. The blue and red circles show the XRT enhanced and the refined *Chandra* positions, respectively. Right panel: image subtraction of the two previous panels, showing the residual afterglow light.

Table 1
Log of Optical and NIR Observations

Date (UT)	Time since Burst (days)	Telescope	Instrument	Filter	Exposure Time (s)	Afterglow Magnitude[a] (AB)	Host Magnitude[a] (AB)
2014 Sep 4.13	0.51	DCT	LMI	r'	300	21.56 ± 0.08	⋯
2014 Sep 4.15	0.53	DCT	LMI	r'	300	21.63 ± 0.06	⋯
2014 Sep 4.22	0.60	Gemini	GMOS	i'	120	21.33 ± 0.05	⋯
2014 Sep 5.18	1.55	DCT	LMI	r'	630	>21.2	⋯
2014 Sep 5.26	1.63	Gemini	GMOS	i'	600	22.99 ± 0.13	⋯
2014 Sep 6.12	2.50	DCT	LMI	r'	600	>22.3[b]	⋯
2014 Sep 6.15	2.52	DCT	LMI	i'	600	>22.0	⋯
2014 Sep 6.17	2.55	DCT	LMI	g'	600	⋯	21.97 ± 0.16
2014 Sep 6.20	2.57	DCT	LMI	z'	600	⋯	19.66 ± 0.08
2014 Sep 6.84	3.22	LT	IO:O	z'	900	>22.5	⋯
2014 Sep 8.12	4.49	DCT	LMI	r'	600	>22.9	⋯
2014 Sep 8.14	4.52	DCT	LMI	i'	340	>21.4	⋯
2014 Sep 8.84	5.22	LT	IO:O	z'	1200	⋯	19.64 ± 0.13
2014 Sep 13.82	10.20	CAHA	Ω_{2000}	J	720	⋯	18.92 ± 0.05
2014 Sep 13.84	10.22	CAHA	Ω_{2000}	H	1200	⋯	18.57 ± 0.07
2014 Sep 13.85	10.23	CAHA	Ω_{2000}	K_s	1800	⋯	18.25 ± 0.05
2014 Sep 23.11	19.49	DCT	LMI	i'	600	>22.9	⋯
2016 Mar 17.92	561	DCT	LMI	r'	880	⋯	20.58 ± 0.09
2016 Mar 18.19	561	DCT	LMI	i'	880	⋯	20.12 ± 0.05
2016 Apr 02.48	577	Gemini	GMOS	i'	600	⋯	20.28 ± 0.09

Notes.
[a] Values not corrected for Galactic extinction.
[b] A faint excess ($r = 23.11 \pm 0.36$) is visible in the residual difference image. Its significance is only marginal ($\lesssim 3\sigma$), and we cannot exclude that it is an artifact of the subtraction method.

sources from SDSS, is presented in Table 1. The transient is detected with high significance in our first epoch at $\Delta t = 12.5$ hr, and possibly at 2.5 days, although the significance of this last detection is only marginal ($\lesssim 3\sigma$).

Using the images from 2016 March 17, we measure the following magnitudes for the underlying host galaxy: $r' = 20.58 \pm 0.09$ and $i' = 20.12 \pm 0.05$. From earlier observations we also measure $g' = 21.97 \pm 0.16$ and $z' = 19.66 \pm 0.08$, although we caution that these fluxes may include some afterglow contribution. The host is unresolved in all of our DCT images (seeing ranging from $0\farcs8$ to $2\farcs0$). Using astrometry from nearby SDSS point sources for reference, we measure a (J2000.0) position of $\alpha = 15^{\rm h}52^{\rm m}03\fs278$, $\delta = +27°36'10\farcs68$. The excess afterglow flux measured in our subtracted images is consistent with this location, within the estimated uncertainty of our astrometric tie (≈100 mas in each coordinate).

2.4. Liverpool and Calar Alto Telescopes

NIR images were acquired in $zJHK_s$ bands using the 2.0 m Liverpool (LT) and the 3.5 m Calar Alto telescopes (CAHA). The LT images were taken in the z band with the IO:O camera, which provides a $10\farcm0 \times 10\farcm0$ field of view and a $0\farcs3$ pixel scale. The CAHA data were acquired in the JHK_s bands with the Ω_{2000} instrument, yielding a $15\farcm4 \times 15\farcm4$ field of view and a $0\farcs45$ pixel scale. In order to reduce the contamination of the nearby bright star, these observations were taken in relatively short (20–30 s) exposures. The reduction followed standard steps: bad pixel masking, bias and flat-field correction, sky subtraction, plus stacking, performed by calling on IRAF tasks (Tody 1993). The resulting photometry, calibrated with respect to nearby point sources from SDSS and the Two Micron All Sky Survey (2MASS; Skrutskie et al. 2006), is presented in Table 1. We used the offsets from Blanton & Roweis (2007) to convert the 2MASS Vega magnitudes to the AB system.

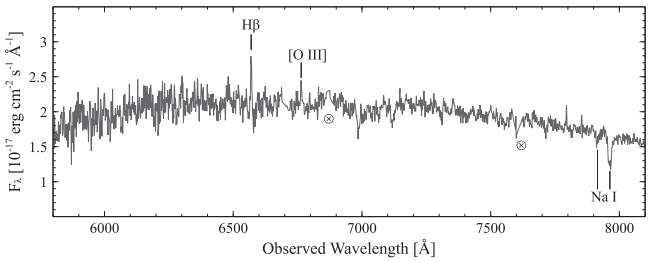

Figure 2. Gemini GMOS spectrum of GRB 140903A and its host galaxy, acquired 14.6 hr after the burst. The positions of detected emission and absorption lines are indicated. Crossed circles mark the position of strong telluric features.

2.5. Gemini Imaging

We imaged the field of GRB 140903A with the Gemini Multi-Object Spectrograph (GMOS; Hook et al. 2004) on the 8 m Gemini North telescope. We obtained a single 120 s i' image beginning at 05:24 UT on 2014 September 4 ($\Delta t = 14.4$ hr) and a dithered sequence of 10×60 s i' exposures at a mean epoch of $\Delta t = 39.2$ hr on 2014 September 5. Our last observation was performed on 2016 April 2 and used as a template for image subtraction. The images were reduced in the standard manner using the `gemini` IRAF package. We performed digital image subtraction on the GMOS images using the same analysis methods as was used for the DCT images (Section 2.3). In the subtracted frame transient emission is clearly detected at an offset of 96 ± 44 mas from the galaxy's center. At a redshift $z = 0.351$ this corresponds to a physical projected offset of 0.5 ± 0.2 kpc. For the transient component we infer $i' = 21.33 \pm 0.05$ mag in our first epoch and $i' = 22.99 \pm 0.13$ mag in the second epoch. This implies a steep temporal decay with slope $\alpha_o = 1.54 \pm 0.15$ between the two observations.

2.6. Gemini Spectroscopy

We obtained a series of spectra of the afterglow+galaxy with GMOS beginning at 05:34 UT on 2014 September 4 ($\Delta t = 14.6$ hr). GMOS was configured with the R400 grating and a central wavelength of 600 nm, providing coverage from $\lambda \approx 4000$ to 8000 Å with a resolution of ≈1000. We restricted our analysis to $\lambda > 5500$ Å due to the poor signal-to-noise ratio of the spectrum at lower wavelengths.

The resulting spectrum is plotted in Figure 2. The strongest (non-telluric) feature is a broad (FWHM ≈ 15 Å) absorption line at $\lambda \approx 7963$ Å, along with a weaker (but still broad, FWHM ≈ 10 Å) absorption line at $\lambda \approx 7915$ Å. We interpret these features as corresponding to Na I with $z \approx 0.35$. We also detect narrow emission lines at $\lambda = 6569.6 \pm 0.5$ Å and $\lambda = 6763.7 \pm 0.6$ Å, which correspond to Hβ and [O III] at $z = 0.351 \pm 0.001$, which we adopt for the redshift of the host.[20] Weak absorption features corresponding to Ca II H + K are also visible at this redshift, though with marginal significance.

2.7. GTC Spectroscopy

Further optical spectroscopy of the host galaxy was performed using OSIRIS (Optical System for Imaging and low Resolution Integrated Spectroscopy; Cepa et al. 2000) at the 10.4 m GTC. Observations started on 2014 October 03, i.e., ∼30.2 days after the trigger, using the R1000B grism (2×600 s exposures) and R2500I VPH (3×600 s exposures). The spectra covered the 3600–7800 Å range at a resolution of ≈1000 and the 7300–10000 Å range at resolution ≈2500. The 1.″0 slit was positioned on the location of the host galaxy, and 2×2 binning mode was used for data acquisition. The obtained spectra were reduced and calibrated following standard procedures using custom tools based in IRAF and Python. Spectra were flux-calibrated using the spectrophotometic standard star GD 248, which was observed during the same night with a 2.″52 slit. In order to account for slit losses, we renormalized the flux of the source to match the DCT magnitudes shown in Table 1. Acquisition images were not usable due to the nearby saturated star.

Although close to a skyline, Hα is clearly detected in the red spectrum at $\lambda = 8862.1 \pm 0.8$ Å, consistent with the redshift from GMOS (Section 2.6). No emission lines are visible in the blue grism spectrum. This may be due to the presence of dust, also suggested by a clear spectral curvature toward the short wavelengths.

Table 2
Log of Radio Observations

Date (UT)	Time since Burst (days)	Frequency (GHz)	Flux (μJy)
2014 Sep 04.06	0.44	6.1	118 ± 11
2014 Sep 06.13	2.51	6.1	203 ± 13
		9.8	153 ± 10
2014 Sep 07.92	4.30	6.1	141 ± 17
2014 Sep 12.89	9.27	6.1	90 ± 20
		9.8	<75
2014 Sep 21.88	18.26	6.1	<130

2.8. Jansky Very Large Array

GRB 140903A was observed with the Jansky Very Large Array (VLA) at both 6.1 GHz (*C* band) and 9.8 GHz (*X* band). Observations started ∼10 hr after the burst and periodically monitored the source for 18 days (Fong et al. 2015). Radio data were downloaded from the public NRAO archive and reduced using the Common Astronomy Software Applications (CASA) v. 4.5.2 package. After standard calibration and basic flagging, we visually inspected the data and applied further screening when needed. Galaxies 3C 286 and J1609+2641 were used as flux and phase calibrators, respectively. The log of radio observations is reported in Table 2. Our values are slightly higher, but largely consistent with those reported by Fong et al. (2015). A simple power-law fit to the data yields decay slopes $\alpha_{6\,\mathrm{GHz}} = 0.63^{+0.14}_{-0.12}$ and $\alpha_{9.8\,\mathrm{GHz}} > 0.5$ for $t > 1$ day. This does not take into account the possible effects of interstellar scintillations (ISSs), which we model in Section 4.2.

3. DATA ANALYSIS

3.1. Gamma-Ray Data

The prompt emission consists of a main Fast Rise Exponential Decay (FRED) pulse, with a duration of $T_{90} = 0.30 \pm 0.03$ s in the 15–350 keV band (Figure 3, left panel). The time-averaged spectrum, from $T + 0.09$ to $T + 0.47$, shows that the prompt emission is well described

[20] The weaker [O III] λ4959 line falls in the chip gap at $z = 0.351$.

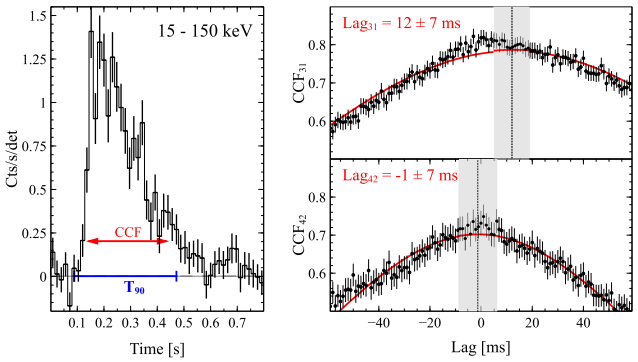

Figure 3. Left panel: BAT light curve of GRB 140903A in the 15–150 keV energy band. The T_{90} time interval and the time interval used for the cross-correlation function (CCF) analysis are shown. Right panel: CCFs between the standard BAT energy bands. The best-fit Gaussian function is reported as a solid line. The lag value and its uncertainties are indicated by the vertical shadowed region.

($\chi^2 = 44$ for 57 degrees of freedom) by a simple power law with $\Gamma = 1.99 \pm 0.08$. According to this best-fit model, the burst fluence in the observed 15–150 keV energy band is $(1.35^{+0.07}_{-0.05}) \times 10^{-7}$ erg cm^{-2}, which, at a redshift $z = 0.351$, corresponds to an isotropic-equivalent energy of $E_{\gamma,\rm iso} = (6.0 \pm 0.3) \times 10^{49}$ erg. Due to the narrow BAT energy bandpass, this only places a lower limit to the bolometric energy release. However, for a typical GRB spectrum (Band et al. 1993), the measured soft photon index indicates that the spectral peak lies close to or within the BAT energy range (Sakamoto et al. 2009). In this case, the bulk of the emission mainly falls within the observed range, and the derived value of $E_{\gamma,\rm iso}$ represents a good estimate of the total energy radiated in the prompt emission.

Spectral lags were calculated by cross-correlating the light curves in the standard BAT channels: 1 (15–25 keV), 2 (25–50 keV), 3 (50–100 keV), 4 (100–350 keV). We followed the method outlined by Ukwatta et al. (2012) and, in order to increase the signal-to-noise ratio in the higher-energy channels, performed the analysis on non-mask-weighted light curves, each with a 4 ms time resolution. The derived lags are $\tau_{31} = 12^{+7}_{-7}$ ms and $\tau_{42} = -1^{+7}_{-7}$ ms, where the quoted uncertainties were derived by Monte Carlo simulations. The results of our lag analysis are shown in Figure 3 (right panel).

We also searched for temporally extended emission following the main burst, but no significant signal was found. By assuming a power-law spectrum with photon index $\Gamma = 2$, we set a 3σ upper limit of 8×10^{-10} erg cm^{-2} s^{-1} (15–50 keV) in the time interval 10–100 s. This is consistent with the MAXI upper limit of 8.4×10^{-10} erg cm^{-2} s^{-1} in the 4–10 keV energy band (Serino et al. 2014).

3.2. X-Ray Data

3.2.1. Spectral Analysis

The afterglow spectral parameters were derived from the time-averaged XRT/PC spectrum (from 100 s to 110 ks). We binned the data in order to have at least 1 count per spectral channel and performed the fit within XSPEC (Arnaud 1996) v.12.9.0 by minimizing the Cash statistic. The spectrum is well described by an absorbed power-law model (W-stat = 329 for 359 degrees of freedom, dof). The best-fit parameters are a photon index $\Gamma_X = 1.66 \pm 0.09$ and an absorbing column $N_{\rm H,int}(z = 0.351) = (1.3 \pm 0.4) \times 10^{21}$ cm^{-2}, in excess of the Galactic value $N_{\rm H,Gal} = 2.9 \times 10^{20}$ cm^{-2} in the burst direction (Kalberla et al. 2005). The adopted value is consistent within errors with the $N_{\rm H,Gal} = 3.3 \times 10^{20}$ cm^{-2} estimated by Willingale et al. (2013).

In our first *Chandra* observation, the source spectrum is well fit (W-stat = 55 for 58 dof) by an absorbed power-law model with $\Gamma_X = 1.8 \pm 0.2$, and $N_{\rm H,\,int} = 1.3 \times 10^{21}$ cm^{-2}, fixed at the value of the XRT best fit. In our second and last *Chandra* observation the low number of counts prevents any spectral analysis. As the hardness ratios of the two *Chandra* observations are consistent within the uncertainties, the same spectral parameters were adopted to estimate the observed flux.

For the best-fit parameters quoted above, we derived an unabsorbed energy conversion factor (ECF) of $(4.8 \pm 0.2) \times 10^{-11}$ erg cm^{-2} count^{-1} for the *Swift*/XRT data and of $(1.40 \pm 0.15) \times 10^{-11}$ erg cm^{-2} count^{-1} for the *Chandra* ACIS-S data.

3.2.2. Temporal Analysis

The X-ray light curve was binned to have a minimum of 15 counts in each temporal bin. The observed count rates were converted into flux units by using the ECFs derived in Section 3.2.1 and by propagating the relative uncertainties. We modeled the afterglow temporal decay with a series of power-law segments ($f_X \propto t^{-\alpha_i}$) and minimized the χ^2 statistics to obtain the best fit to the data. The afterglow displays a shallow decay phase with temporal index $\alpha_1 \sim 0.2$, which steepens to $\alpha_2 \sim 1.1$ after $t_{bk,1} \sim 7$ ks. Our first *Chandra*/ACIS-S data point lies below the predictions based on the *Swift*/XRT data set, hinting at a second temporal break in the light curve. However, the combined XRT/ACIS-S data set could be reasonably well described by adopting a steeper temporal index $\alpha_2 \sim 1.5$ for the final power-law decay and no additional break. A second *Chandra* observation was therefore executed in order to distinguish between the two models. This last measurement confirms the presence of an additional break in the X-ray light curve at a time $t_j \approx 1$ day and allows us to constrain the slope of the final decay to $\alpha_3 \sim 2.1$. The best-fit temporal models are summarized in Table 3. The X-ray light curve and our best-fit model are presented in Figure 4 and compared to the optical (Table 1) and radio measurements (Table 2) in order to highlight the achromatic nature of the last temporal break t_j, which we interpret as the jet-break time.

3.3. Afterglow Spectral Energy Distribution

In order to study the spectral evolution across the temporal break t_j detected in X-rays, we extracted the afterglow spectral energy distribution (SED) at two different epochs, $t_1 = 0.5$ days ($<t_j$) and $t_2 = 2.5$ days ($>t_j$). These times were selected in order to maximize the simultaneous coverage at different wavelengths.

Optical fluxes were derived by the best-fit temporal model in Table 3 and corrected for Galactic extinction in the GRB direction ($E_{B-V} \approx 0.03$; Schlegel et al. 1998). A power-law fit ($f_\nu \propto \nu^{-\beta}$) to the optical and X-ray data yields spectral slopes $\beta_{OX} = 0.72 \pm 0.05$ at $t = t_1$, $\beta_{OX} = 0.76 \pm 0.12$ at $t = t_2$, significant intrinsic absorption $N_{\rm H} = (1.8 \pm 0.4) \times 10^{21}$ cm^{-2}, and marginal evidence of dust extinction $A_V = 0.47 \pm 0.25$. The simple power-law fit provides a good description of the

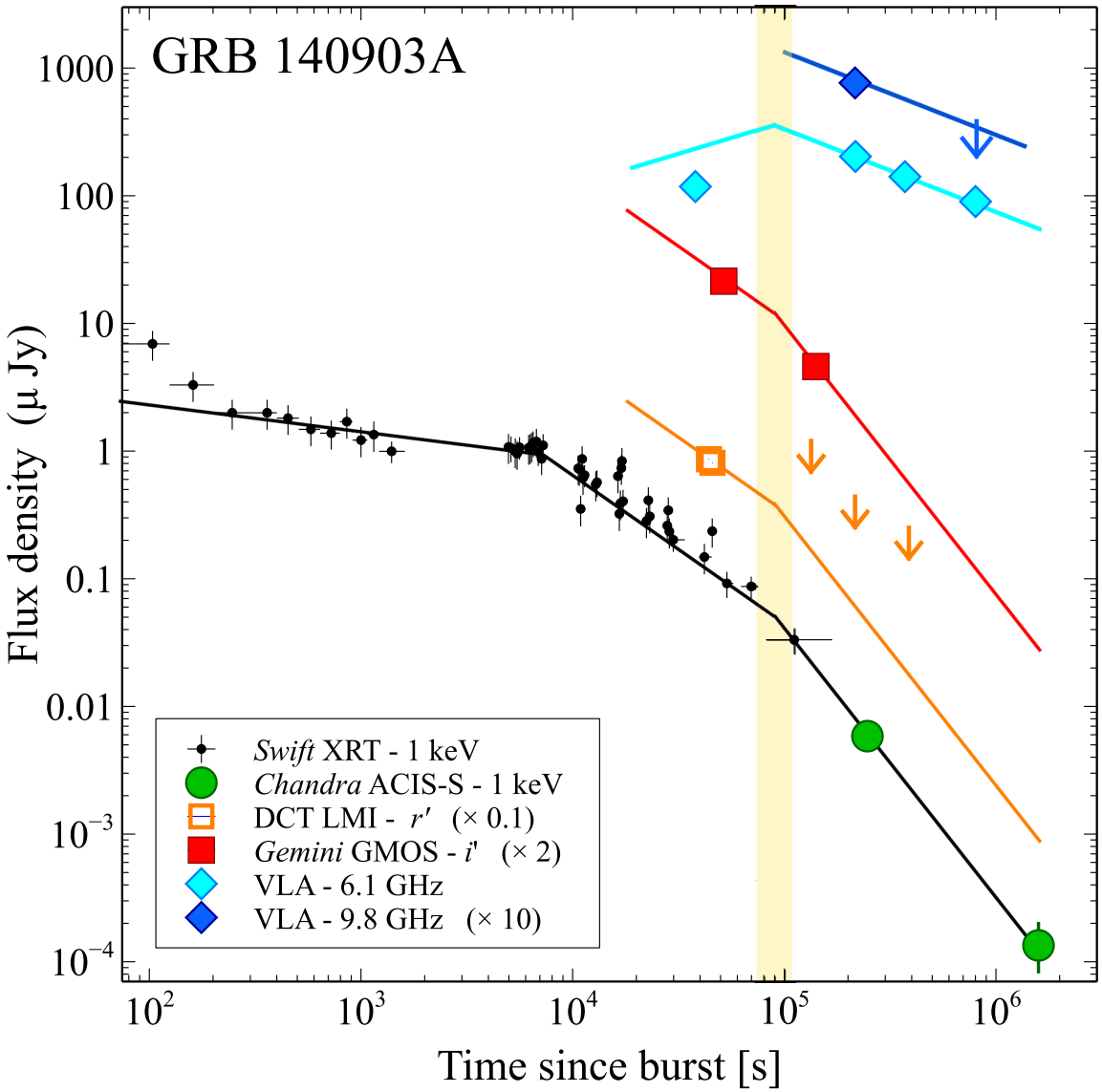

Figure 4. Afterglow light curves of GRB 140903A, combining X-ray data from *Swift*/XRT (small circles) and *Chandra*/ACIS-S (large circles), optical data from DCT (open squares) and Gemini (filled squares), and radio data from the VLA (diamonds). Error bars are 1σ, and arrows denote 3σ upper limits. The best-fit temporal model is shown as a solid line. The vertical band marks the time of the jet break.

Table 3
Afterglow Light-curve Fit Parameters

Band	α_1	$t_{bk,1}$ (ks)	α_2	$t_{bk,2}$ (ks)	α_3	χ^2/dof
X	0.20 ± 0.02	$7.3^{+0.6}_{-0.9}$	$1.06^{+0.07}_{-0.11}$	69^{+17}_{-12}	$2.11^{+0.22}_{-0.07}$	43/46
O	1.54 ± 0.15	…	…	…	…	…
$X + O$	0.21 ± 0.02	$7.9^{+1.0}_{-0.9}$	$1.16^{+0.10}_{-0.03}$	89^{+11}_{-12}	$2.1^{+0.2}_{-0.2}$	49/48
R (6.1 GHz)	-0.5[a]	89^{+11}_{-12}	0.63 ± 0.14	…	…	…
R (9.8 GHz)	>0.5	…	…	…	…	…

Note.
[a] The temporal slope was held fixed at the value predicted by the standard fireball model for $\nu_{sa} < \nu < \nu_m$.

data set (W-stat = 355 for 371 dof), suggesting that optical emission and X-ray emission belong to the same spectral segment ($\nu_m < \nu_{opt} < \nu_X < \nu_c$) of the synchrotron spectrum. The lack of significant spectral variation across the temporal break t_j is consistent with the properties of a jet break and excludes alternative interpretations (e.g., cooling frequency).

By extrapolating the observed spectrum to radio energies, the predicted flux at $t = t_1$ is ≈10 mJy, two orders of magnitude

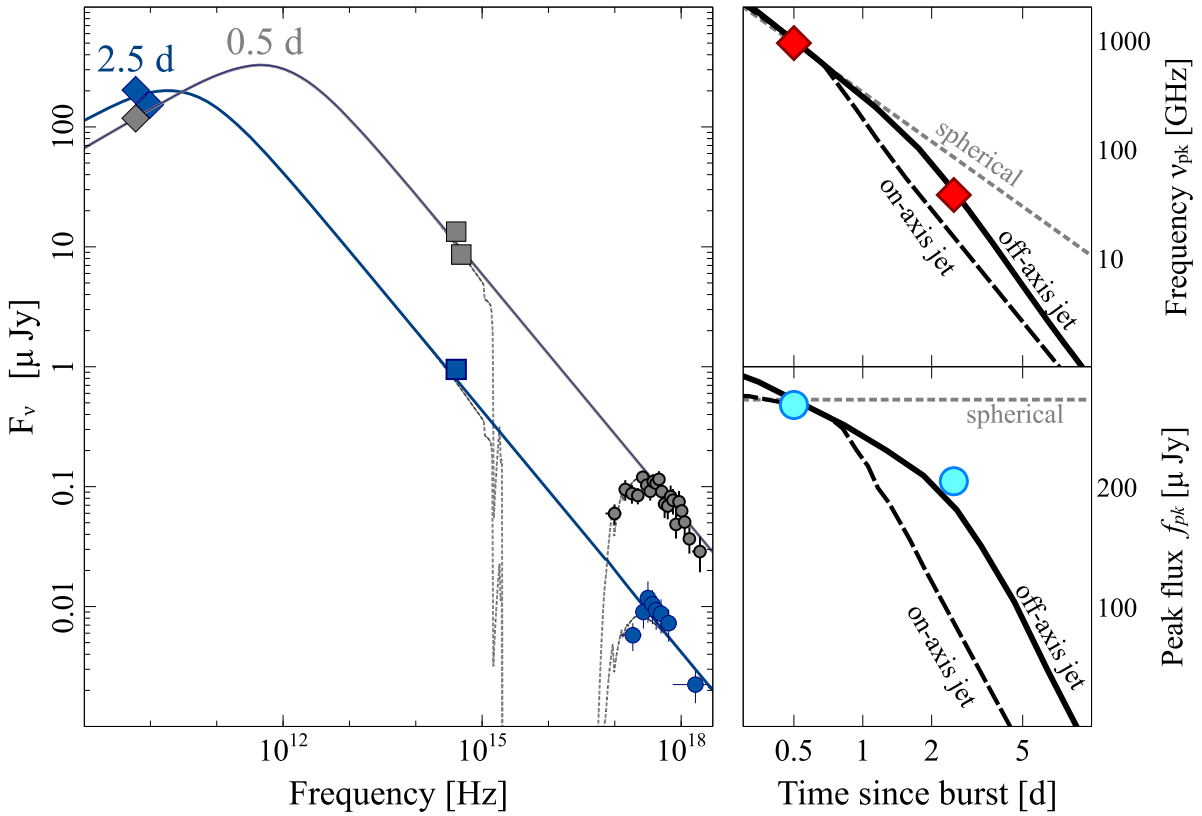

Figure 5. Left panel: afterglow SED at two different epochs, $t_1 = 0.5$ days before the jet break and $t_2 = 2.5$ days after the jet break. We fit the broadband spectrum with a smoothly broken power law; our best-fit models are shown by the solid lines. The thin dotted lines show the effects of absorption and extinction. Top right panel: temporal evolution of the peak frequency across the jet break. We report the expected behavior for three different models: the spherical fireball (dotted line), a narrow jet ($\theta_{jet} = 0.1$ rad) seen on-axis (dashed line), and one seen slightly off-axis ($\theta_{obs}/\theta_{jet} = 0.6$; solid line). Our measurements, indicated by the red diamonds, agree well with the off-axis jet model. Bottom right panel: same as above but for the spectral peak flux. Also in this case, our derived values (cyan circles) agree well with the trend expected from an off-axis jet.

higher than the radio measurement. This implies a spectral break between the optical and radio band, and that the radio data belong to a different spectral segment ($\nu_r < \nu_m$). By adopting the standard closure relations for GRB afterglows (Zhang & Mészáros 2004), we fixed the radio spectral index to $\beta_r = 1/3$ and fitted the broadband SED with a smoothly broken power law. We added to the model a systematic uncertainty in order to take into account the possible effects of interstellar scattering and scintillation at radio wavelengths. Although a proper estimate of the ISS fluctuations requires more complex modeling (see Section 4.2), at this stage we introduce an uncertainty of ≈30%. Our fit constrains the spectral peak to lie in the IR region at $\nu_{pk} \approx 9.3 \times 10^{11}$ Hz at 0.5 days. At our second epoch, the radio measurements are only slightly lower than the extrapolation of the higher-energy spectrum, implying that the spectral peak moved close to the radio band. We estimate $\nu_{pk} \approx 37$ GHz at 2.5 days, above the VLA frequencies. This shows that the observed radio, optical, and X-ray emission remained in the same spectral regime; thus, the observed temporal break was not caused by spectral variations. Basic considerations on the spectral and temporal behavior of the afterglow disfavor a wind-like environment, which would cause a steeper decay ($\alpha_{wind} \approx 1.5$) of the pre-break X-ray afterglow. Our analysis also shows that the broadband spectrum evolved in time as $\nu_{pk} \propto t^{-2}$ and $f_{pk} \propto t^{-0.3}$. As shown in Figure 5 (right panels), these decay rates are significantly steeper than the ones predicted by the spherical fireball model for a uniform medium, and are instead consistent with the spectral evolution of a collimated outflow. In particular, the slow decay of the peak flux strongly favors a narrow jet model seen slightly off-axis.

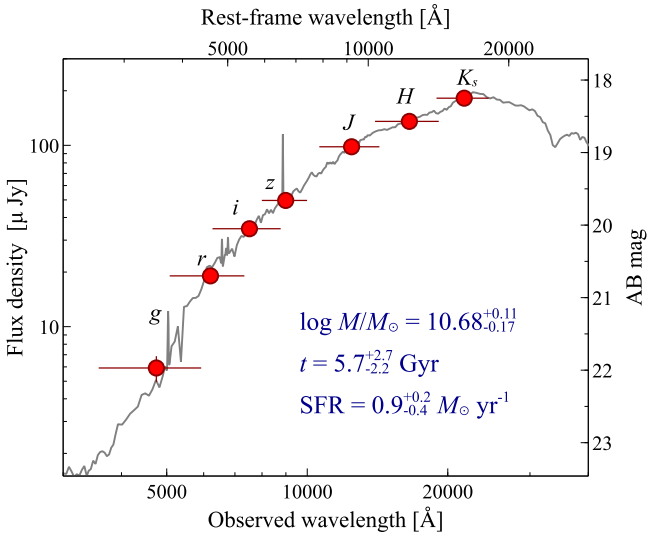

Figure 6. Photometry of the galaxy hosting GRB 140903A. Data (filled circles) are corrected for Galactic extinction in the direction of the GRB. The best-fit stellar population synthesis model (gray curve) and its parameters are reported.

3.4. Host Galaxy Properties

GRB 140903A is located on top of a compact and red galaxy, suggestive of an old system. Based on the galaxy sky densities in the r band (Yasuda et al. 2001), we estimated a small probability of a chance association, $P_{\rm ch} \approx 3 \times 10^{-4}$ (Bloom et al. 2002; Troja et al. 2008), and we therefore consider this galaxy as the GRB host. From our r-band measurement we derive a rest-frame absolute B-band magnitude $M_B \approx -20.9$ mag, or $L_B \approx 0.8 L_*$ when compared to the luminosity function of galaxies at a similar redshift $0.2 < z < 0.4$ (Willmer et al. 2006). In order to characterize the galaxy's physical properties, we used the late-time ($t > 3$ days) optical and IR data to build the host galaxy SED, and we ran a photometric fit with a grid of spectral templates within LEPHARE v. 2.2 (Ilbert et al. 2006). The templates were created using the stellar population synthesis libraries of Bruzual & Charlot (2003) with the Padova 1994 evolutionary tracks, and assuming the initial mass function (IMF) from Chabrier (2003). We adopted an exponential star formation history with different e-folding times τ and included the contribution of emission lines following Kennicutt (1998).

Our results are shown in Figure 6. Our best-fit model (gray curve) well reproduces the optical and NIR continua. The best-fit parameters for the galaxy template are an intrinsic extinction $E_{B-V} = 0.25$, solar metallicity, e-folding time $\tau = 500$ Myr, stellar mass $\log(M/M_\odot) = 10.61 \pm 0.15$, an old stellar age $t = 4.1^{+3.9}_{-2.3}$ Gyr, and a moderate star formation rate SFR $= 1.0 \pm 0.3\, M_\odot\, {\rm yr}^{-1}$, in agreement with the presence of nebular emission lines in our spectra.

By using the extinction-corrected Hα line flux, we infer a comparable value of SFR $= 0.38 \pm 0.04\, M_\odot\, {\rm yr}^{-1}$ (Kennicutt 1998) for a Chabrier IMF and a specific SFR of $0.47 \pm 0.05\, (L/L_*)\, M_\odot\, {\rm yr}^{-1}$. Based on the diagnostic $F([{\rm O\,III}]\, \lambda 5007)/F({\rm H}\beta) \sim 0.48$ (Nagao et al. 2006), we estimate a supersolar metallicity $12 + \log({\rm O/H}) \approx 9.0 \pm 0.2$, not unprecedented among short GRB host galaxies (Perley et al. 2012).

4. RESULTS

4.1. Origin of the X-Ray Emission

The early X-ray afterglow of GRB 140903A is characterized by a period of fairly constant emission lasting ≈4 hr. The shallow decay slope $\alpha_1 \sim 0.2$ is not consistent with a standard forward shock origin, and this is often considered a sign of prolonged energy injection into the blast wave (Fan & Xu 2006; Zhang et al. 2006; Cannizzo et al. 2011). Indeed, it has been suggested that in a significant fraction of GRBs the X-ray plateaus originate from the internal dissipation of the engine-driven wind rather than from shocks at an external radius. In this scenario, known as "internal plateau" (Troja et al. 2007), the forward shock component is subdominant, and the observed X-ray emission is *directly* powered by the central engine. One of the most popular models invokes a newborn magnetar as the power source of the GRB and its afterglow: as the magnetar spins down, it injects energy into the jet, causing a period of nearly flat emission (the plateau), followed by a steeper temporal decline with slope $\alpha \gtrsim 2$ (Zhang & Mészáros 2001). This rapid decay may mimic the presence of a jet break, complicating the interpretation of the observed X-ray emission.

In the case of GRB 140903A, the standard expression for magnetic dipolar radiation (Shapiro & Teukolsky 1983) provides an excellent description of the X-ray data set, as it can fully account for the two salient features of the observed light curve—a short-lived plateau and a final steep decay—with the advantage of only two free parameters. However, due to the small radius at which the internal dissipation occurs, a bright optical and radio counterpart is not expected in these cases. Indeed, a distinctive feature of "internal plateaus" is that they appear as achromatic bumps visible in X-rays, but not at lower energies (Troja et al. 2007; Lyons et al. 2010; Rowlinson et al. 2013). Our SED analysis showed instead that X-ray, optical, and radio data are consistent with being from the same emission component. In particular, by considering that the radio data lie above the self-absorption frequency ν_a, we can derive a rough estimate of the emitting radius $R \gtrsim 4 \times 10^{16}$ cm at $t = 0.5$ days (Barniol Duran et al. 2013), consistent with an external shock origin. Moreover, the observed temporal and spectral indices ($\beta_{OX} \approx 0.7$, $\alpha_2 \approx 1.1$) after the plateau phase are in agreement with the canonical closure relations for $\nu_m < \nu_X < \nu_c$ and $p \approx 2.4$. Based on these considerations, we favor an external origin for the observed X-rays. In this scenario, the X-ray plateau is *indirectly* powered by the central engine via sustained energy injection into the forward shock, and after the cessation of energy injection is communicated to the shock front, the afterglow evolves in a standard fashion (van Eerten 2014). Therefore, the X-ray emission is not directly linked to the time history of the central engine; instead, it carries important information about the jet collimation, energetics, and surrounding environment.

4.2. Afterglow Modeling

We modeled the broadband data set (from radio to X-rays) by using the standard prescriptions for an expanding spherical fireball and the scaling relations for the post-jet-break evolution (Sari et al. 1999). We excluded from the fit the early-time data ($t < t_{bk,1}$) as they are affected by persistent energy injection. In our fit we implemented a routine to calculate the expected ISS modulation for each set of input afterglow parameters. By adopting the "NE2001" model (Cordes & Lazio 2002), we derived a scattering measure ${\rm SM} = 1.3 \times 10^{-4}\, {\rm kpc/m}^{-20/3}$ and a transition frequency $\nu_0 = 8$ GHz in the direction of GRB 140903A. Observations below this frequency could possibly be affected by strong scattering if the source size is smaller than the ISS angular scale, $\theta_{F0} \approx 1\ \mu$as. At the GRB redshift this corresponds to an apparent fireball size $R_\perp \lesssim 2 \times 10^{16}$ cm, which is likely the case at the early timescales here considered. The derived ISS fluctuations were treated as a source of systematic uncertainty and added in quadrature to the statistical errors when evaluating the fit statistics.

We assumed a uniform circumburst medium with density n_0 and constant microphysical parameters ϵ_e and ϵ_B. Under these assumptions, we did not find an acceptable fit to the data ($\chi^2 = 65$ for 43 dof), mainly because the model predicts a much faster decay of the peak flux and peak frequency after the jet break. We attempted to model this effect by leaving the microphysical parameters free to vary in time as $\epsilon_e \propto t^e$ and $\epsilon_B \propto t^b$. Although the fit formally improves for $b \approx 0.5$ and $e \approx 0.2$, it yields an unphysical solution $\epsilon_e > 1$ and extreme values for the blast-wave kinetic energy and the jet opening angle. We considered this model an unrealistic description of

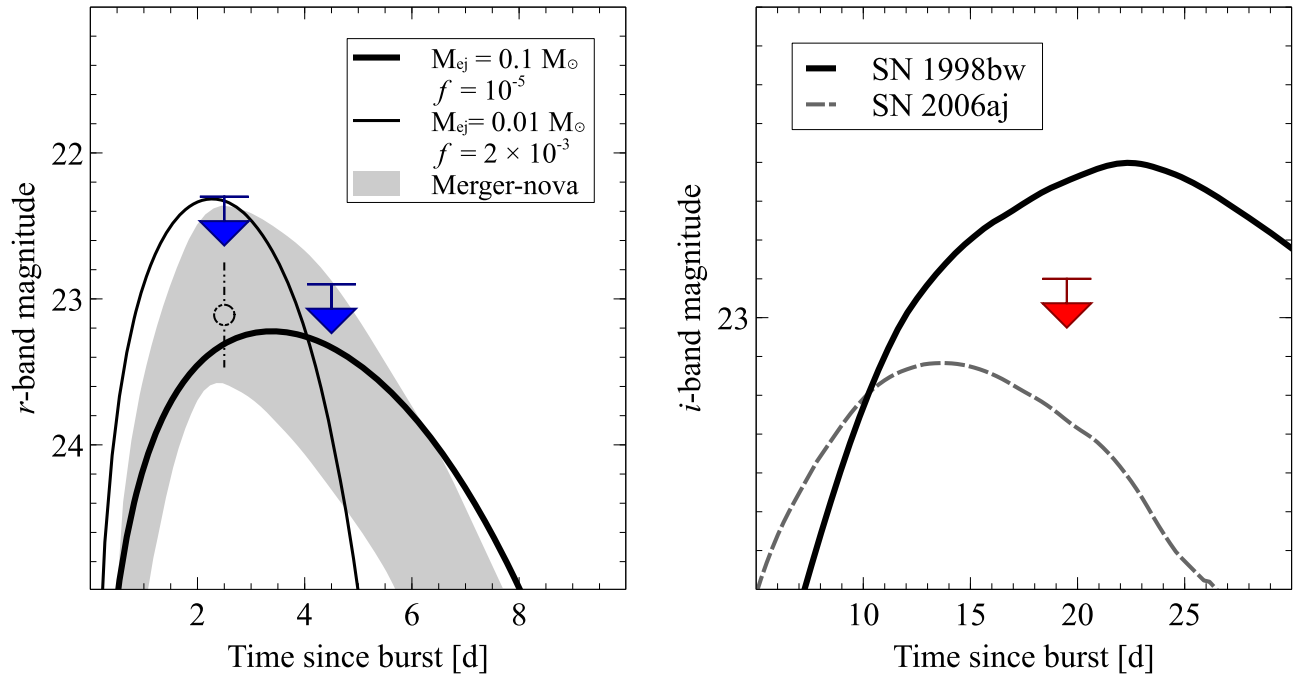

Figure 7. Left panel: late-time r-band upper limits compared with theoretical light curves of a macronova (solid lines) and a magnetar-driven merger-nova (shaded area). The dot-dashed symbol shows the low-significance signal visible in our DCT image at 2.5 days. The macronova signal was derived by using the following parameters: a lanthanide-free opacity $\kappa = 1\ \mathrm{cm^2\ g^{-1}}$, ejecta velocity $v = 0.1\ c$, ejecta mass $M_{ej} = 0.01\ M_\odot$, and a rather high radioactive energy deposition $f = 2 \times 10^{-3}$ (thin solid line); $\kappa = 1\ \mathrm{cm^2\ g^{-1}}$, $v = 0.1\ c$, $M_{ej} = 0.1\ M_\odot$, and $f = 10^{-5}$ (thick solid line). The merger-nova model was calculated by assuming a long-lived stable magnetar and ejecta masses $10^{-4}\ M_\odot < M_{ej} < 10^{-2}\ M_\odot$ (dashed line). We applied to the models an extinction term as derived from the afterglow fit. Right panel: late-time i-band observations compared with the extinction-corrected template light curves of GRB SNe: SN 1998bw (solid line) and SN 2006aj (dashed line).

the explosion and turned to a different interpretation to explain the observed properties.

As shown in Figure 5 (right panels), the temporal evolution of the broadband spectrum appears roughly consistent with a collimated fireball observed slightly off-axis. We therefore introduced in our model the effects of different viewing angles (van Eerten et al. 2010; van Eerten & MacFadyen 2013). This provides a better description of the observed data. The best-fit parameters are an isotropic-equivalent kinetic energy $E_{K,iso} = 4.3^{+1.2}_{-2.0} \times 10^{52}$ erg, a circumburst density $n_0 = 0.032^{+0.14}_{-0.026}\ \mathrm{cm^{-3}}$, and shock parameters $\epsilon_B = 2.1^{+3.6}_{-1.4} \times 10^{-4}$, $\epsilon_e = 0.14^{+0.19}_{-0.06}$. We derived a jet opening angle of $\theta_j = 0.090 \pm 0.012$ rad and an observer's angle of $\theta_{obs} \approx 0.055$ rad. These values are similar to the opening angles inferred from other candidate jet breaks (Burrows et al. 2006; Coward et al. 2012; Fong et al. 2015).

4.3. Constraints on Supernova-like Transients

The possibility of an optical/IR transient rising a few days after the short GRB explosion is the current focus of intense research (e.g., Barnes & Kasen 2013; Yu et al. 2013; Kasen et al. 2015). The detection and identification of such transients (e.g., Tanvir et al. 2013; Jin et al. 2015, 2016; Yang et al. 2015) would represent the smoking gun proof of short GRB progenitors and a powerful tool to search for electromagnetic counterparts of GW sources. We used our late-time observations to constrain some of the most promising models, as well as the presence of an emerging supernova (SN).

As shown in Figure 7 (left panel), our r-band upper limits at 2.5 and 4.5 days can constrain the presence of a fast-rising and rapidly decaying transient, peaking in the optical a few days after the burst. We considered two models: the classical Li & Paczyński (1998) macronova (or kilonova) powered by the radioactive decay of the ejecta (shaded area), and the more recent merger-nova (Yu et al. 2013) powered by a long-lived magnetar (shaded area). Recent theoretical (Barnes & Kasen 2013) and observational (Tanvir et al. 2013) results showed that the macronova emission is heavily suppressed at optical wavelengths due to the high opacity of the ejecta. Models for the late-time infrared emission (e.g., Barnes & Kasen 2013), although highly dependent on the input physics, generally predict a signal ($H \gtrsim 23$ mag at $t \sim 4$ days) well below the sensitivity of our observations. However, exceptions may occur if a small amount of lanthanide-free material is ejected during the merger (Kasen et al. 2015) or if the ejecta are re-energized by the central engine (Yu et al. 2013). The resulting transient spans a wide range of luminosities depending on the details of the explosion, and our measurements can only constrain the bright end of the predicted values. For a Li & Paczyński (1998) macronova with a typical ejecta mass of $M_{ej} = 0.01\ M_\odot$ (thin solid line) we can exclude only the extreme values of the f parameter ($f > 2 \times 10^{-3}$), which measures the fraction of radioactive material converted into heat. Our limit is more interesting in the case of a larger ejecta mass of $M_{ej} = 0.1\ M_\odot$, for which we can exclude $f > 10^{-5}$ (thick solid line). This is consistent with the most recent calculations of the radioactive heating rate (Metzger et al. 2010; Lippuner & Roberts 2015).

Yu et al. (2013) argued that, if the GRB central engine is a stable magnetar, the macronova luminosity could be boosted by several orders of magnitude. In this scenario, the main power

source is the magnetar-driven wind rather than the radioactive decay energy. As shown in Figure 7, for a typical range of ejecta masses ($M_{\rm ej} \lesssim 10^{-2}\,M_{\odot}$) the predicted signal of a merger-nova (dashed line) could be consistent with our observations.

As mentioned in Section 2.3, we found marginal ($\lesssim 3\,\sigma$) evidence of a signal in our observations 2.5 days post burst. The resulting magnitude, $r = 23.11 \pm 0.36$, is above the predicted afterglow signal and, if real, would imply an optical rebrightening between our *Gemini* observations at 1.5 days and the DCT observations at 2.5 days. When compared with the macronova predictions, this signal would require either an extreme value of the *f*-parameter $5 \times 10^{-4} < f < 10^{-3}$ for $M_{\rm ej} = 0.01\,M_{\odot}$ or a large ejecta mass, $M_{\rm ej} = 0.1\,M_{\odot}$, and $f \sim 10^{-5}$, more typical of a neutron star (NS)–black hole (BH) merger (Foucart et al. 2014). The merger-nova predictions could instead reproduce the observed flux for ejecta masses $M_{\rm ej} \approx 10^{-3}\,M_{\odot}$, typical of NS–NS mergers (Bauswein et al. 2013).

Our last *i*-band observation, performed 3 weeks after the burst, is used to constrain the contribution of a possible SN. In Figure 7 (right panel) we compare our upper limit with the light curves of SN 1998bw and SN 2006aj, associated to nearby long GRBs. The templates were created by compiling data from literature (Galama et al. 1998; Ferrero et al. 2006) and then corrected for cosmological effects and extinction in a standard fashion. Our limit ($M_V \gtrsim -19$ mag, rest frame) is fainter than the emission expected from an SN 1998bw-like explosion. Although our photometric data set cannot exclude an event such as SN 2006aj, we also note that the spectroscopic observations do not show any evidence of broad absorption lines typical of GRB SNe.

5. DISCUSSION

We have presented several lines of evidence linking GRB 140903A to the class of short-duration GRBs (Kouveliotou et al. 1993), and in support of the popular compact binary merger model. Although characterized by a rather soft spectrum with photon index $\Gamma \sim 2$, the GRB prompt emission displays a very short duration ($T_{90} \sim 0.3$ s), negligible spectral lags, and a low luminosity ($L_{\gamma,\rm iso} \sim 10^{50}$ erg s^{-1}), all key features of the class of short GRBs (Gehrels et al. 2006; Norris & Bonnell 2006). The GRB afterglow was found on top of a relatively bright galaxy. Given the accurate afterglow localization, the probability of a chance alignment can be considered negligible ($P_{\rm ch} \approx 0.03\%$). Moreover, the galaxy's properties (stellar mass, age, and metallicity) are broadly consistent with the population of short GRB host galaxies (D'Avanzo et al. 2009; Savaglio et al. 2009; Berger 2014). Both the environment and the lack of a bright SN (Section 4.3) disfavor a massive star progenitor and support instead the merger model for GRB 140903A.

Direct evidence of an NS merger progenitor would be the detection of an *r*-process macronova (Li & Paczyński 1998). Our observations constrain only a limited range of the parameter space, and for the most likely values of ejecta masses and heating fraction, our upper limits are consistent with theoretical predictions. A marginal detection in the residual image at 2.5 days could fit well the expected emission from a magnetar-driven macronova (or merger-nova; Yu et al. 2013). Unfortunately, given the low significance of the detection, the lack of confirmation in other bands, and the complexity of the field, we cannot exclude that the observed feature is an artifact of the subtraction process. Although this does not allow us to draw any robust conclusion on this particular event, it shows that rapid and deep observations of short GRBs with large-aperture telescopes are fundamental in order to pin down the possible onset of a macronova.

The most remarkable feature of this afterglow is the detection of an achromatic break at $t_j \approx 1$ day followed by a steep decay of the X-ray flux. Several mechanisms have been suggested to explain a rapid decay of the X-ray afterglow (e.g., Zhang & Mészáros 2001; Troja et al. 2007; van Eerten 2014), although most of them predict a chromatic break preceding the steep flux decay. An achromatic break could be due to the cessation of energy injection. However, our analysis showed that the pre-break afterglow is consistent with the standard closure relations (Zhang & Mészáros 2004) without energy injection. We therefore interpret the observed break as evidence of a collimated outflow. Although early studies suggested the production of relatively wide outflows from NS mergers (Ruffert & Janka 1999; Aloy et al. 2005), more recent works show that confinement from either the poloidal magnetic field (Rezzolla et al. 2011) or the expanding cloud of ejecta (Nagakura et al. 2014; Duffell et al. 2015) can produce a jet-like structure. Our observations of GRB 140903A add compelling evidence that at least some short GRBs are beamed into narrow jets.

In Section 4.2 we constrained the basic properties of the jet: an opening angle $\theta_j \approx 5°$, an isotropic-equivalent energy release $E_{\rm K,iso} \approx 4 \times 10^{52}$ erg, and a viewing angle $\theta_{\rm obs} \approx 3°$. Our modeling yields a blast-wave kinetic energy that is significantly higher than the observed prompt gamma-ray energy. This would imply an unusually low radiative efficiency, $\eta_\gamma \approx 0.2\%$. However, since we observed the explosion slightly off-axis, the faint prompt emission could be due to a viewing angle effect: if the GRB jet is characterized by a compact central core and a steep radial gradient (Janka et al. 2006), an off-axis observer would indeed measure a dimmer and spectrally softer burst.

The beaming factor $f_b \sim 250$ has a direct impact on the GRB energy release and true event rate and therefore on the progenitor models. Coward et al. (2012) estimate the observed rate of short GRBs as $\sim 8\,{\rm Gpc^{-3}\,yr^{-1}}$. Collimation can boost this number up to $\sim 2 \times 10^3\,{\rm Gpc^{-3}\,yr^{-1}}$, which is consistent with the conservative rate density of NS–NS mergers from Abadie et al. (2010). This would suggest that most NS mergers successfully launch a short GRB, and that other systems, such as NS–BH or white dwarf binaries, do not contribute significantly to the observed GRB population. An important caveat to the above comparison between observations and progenitor models is that estimates of GRB jet angles are unavoidably biased by our observing strategy and limited sensitivity. Narrowly collimated jets, if pointed toward us, are more likely to trigger *Swift* over a larger volume and to produce bright afterglows, allowing for the jet-break detection. On the other hand, wide outflows of comparable energy produce dimmer GRBs and afterglows, which are harder to detect and characterize. A proper assessment of the GRB event rate should properly account for these observational biases.

The collimation-corrected energy release is $E \approx 2 \times 10^{50}$ erg, which is in the typical range for short GRBs and lower than average long-duration bursts (Cenko et al. 2010; Zhang et al. 2015). Recently, Perna et al. (2016) proposed a new mechanism to power a short GRB from a BH–BH

collision. However, the low disk mass available in this system could only power a faint, low-luminosity transient, not consistent with the energetics measured in our case. GRB 140903A was more likely produced by a merger event in which at least one of the two compact objects was a neutron star. According to the standard NS merger model, a stellar-mass black hole surrounded by a hot massive torus is formed after the merger. Energy is extracted from this system through neutrino-antineutrino annihilation or magnetically driven mechanisms. Pair annihilation of neutrinos and antineutrinos can supply an energy deposition rate $L_{\nu\bar{\nu}} \lesssim 10^{51}\,\mathrm{erg\,s^{-1}}$ (Setiawan et al. 2004; Birkl et al. 2007), consistent with the energy budget of GRB 140903A. Following the formalism of Fan & Wei (2011), we use the burst energetics to estimate a post-merger disk mass $M_{\rm disk} \approx 0.1\,M_{\odot}$. This is in agreement with numerical simulation of merging NS–NS and NS–BH binaries. If instead the outflow is driven by more efficient magnetic processes, the disk mass could be as low as $10^{-3}\,M_{\odot}$, suggesting a high-mass binary NS merger (Giacomazzo et al. 2013). An alternative scenario is the formation of a supramassive and highly magnetized neutron star after the merger (Giacomazzo & Perna 2013). In this case, there are less robust predictions connecting the central engine and the GRB observed properties. A general requirement is that the total energy release should not exceed the maximum rotational energy of the newborn NS, $E_{\rm rot} \approx 10^{53}(M_{\rm NS}/2\,M_{\odot})^{3/2}$ erg. The burst energetics are well below this limit and consistent with the proto-magnetar model. A compact binary merger can therefore naturally explain the observed GRB properties, although the nature of the central engine and the energy extraction mechanisms remain uncertain. Only future detections of GW radiation will be able to ultimately discriminate between these different scenarios.

6. CONCLUSIONS

We detected a temporal break in the X-ray afterglow light curve of the short GRB 140903A. The afterglow temporal decay was observed to steepen from $\alpha_1 \sim 1.1$ to $\alpha_2 \sim 2.1$, suggesting the presence of a jet break at $t_j \approx 1$ day after the burst. Simultaneous observations at optical and radio wavelength showed that the break is achromatic. This disfavors a large set of models, including the magnetar-powered "internal plateau," which are expected to produce a chromatic break. Instead, we showed that the observed afterglow is consistent with the standard forward shock emission from a narrow jet expanding into a homogeneous medium. We measure a jet opening angle of 5°, an observer's angle of 3°, and a total energy release of 2×10^{50} erg. Several lines of evidence link this event to the popular NS merger scenario: the prompt gamma-ray emission, the environment, the lack of a bright SN, the energetics, and the rate of events. Our results show that NS mergers can produce highly collimated outflows.

The scientific results reported in this article are based in part on observations made by the *Chandra X-ray Observatory*. Support for this work was provided by the National Aeronautics and Space Administration through *Chandra* Awards GO4-15072A and GO4-15067A issued by the Chandra X-ray Center, which is operated by the Smithsonian Astrophysical Observatory for and on behalf of the National Aeronautics Space Administration under contract NAS8-03060. These results also made use of Lowell Observatory's Discovery Channel Telescope. Lowell operates the DCT in partnership with Boston University, Northern Arizona University, the University of Maryland, and the University of Toledo. Partial support of the DCT was provided by Discovery Communications. LMI was built by the Lowell Observatory using funds from the National Science Foundation (AST-1005313). This paper is partly based on observations obtained at the Gemini Observatory, which is operated by the Association of Universities for Research in Astronomy, Inc., under a cooperative agreement with the NSF on behalf of the Gemini partnership: the National Science Foundation (United States), the National Research Council (Canada), CONICYT (Chile), Ministerio de Ciencia, Tecnología e Innovación Productiva (Argentina), and Ministério da Ciência, Tecnologia e Inovação (Brazil). Observations were also carried out with the 10.4 m Gran Telescopio Canarias installed in the Spanish Observatorio del Roque de los Muchachos of the Instituto de Astrofisica de Canarias in the island of La Palma (GTC59-14B) and with the 3.5 m CAHA telescope at the German-Spanish Calar Alto Observatory operated by the IAA-CSIC. A.J.C.T. acknowledges support from the Spanish Ministry Projects AYA2012-39727-C03-01 and 2015-71718R.

REFERENCES

Abadie, J., Abbott, B. P., Abbott, R., et al. 2010, CQGra, 27, 173001
Abbott, B. P., Abbott, R., Abbott, T. D., et al. 2016a, ApJL, 826, L13
Abbott, B. P., Abbott, R., Abbott, T. D., et al. 2016b, PhRvL, 116, 061102
Ahn, C. P., Alexandroff, R., Allende Prieto, C., et al. 2014, ApJS, 211, 17
Aloy, M. A., Janka, H.-T., & Müller, E. 2005, A&A, 436, 273
Antonelli, L. A., D'Avanzo, P., Perna, R., et al. 2009, A&A, 507, L45
Arnaud, K. A. 1996, in ASP Conf. Ser. 101, Astronomical Data Analysis Software and Systems V, ed. G. H. Jacoby & J. Barnes, (San Francisco, CA: ASP), 17
Band, D., Matteson, J., Ford, L., et al. 1993, ApJ, 413, 281
Barnes, J., & Kasen, D. 2013, ApJ, 775, 18
Barniol Duran, R., Nakar, E., & Piran, T. 2013, ApJ, 772, 78
Barthelmy, S. D., Barbier, L. M., Cummings, J. R., et al. 2005, SSRv, 120, 143
Bauswein, A., Goriely, S., & Janka, H.-T. 2013, ApJ, 773, 78
Becker, A. 2015, Astrophysics Source Code Library, ascl:1504.004
Berger, E. 2014, ARA&A, 52, 43
Bertin, E. 2006, in ASP Conf. Ser. 351, Astronomical Data Analysis Software and Systems XV, ed. C. Gabriel et al. (San Francisco, CA: ASP), 112
Bertin, E., Mellier, Y., Radovich, M., et al. 2002, in ASP Conf. Ser. 281, Astronomical Data Analysis Software and Systems XI, ed. D. A. Bohlender, D. Durand, & T. H. Handley (San Francisco, CA: ASP), 228
Birkl, R., Aloy, M. A., Janka, H.-T., & Müller, E. 2007, A&A, 463, 51
Blanton, M. R., & Roweis, S. 2007, AJ, 133, 734
Bloom, J. S., Kulkarni, S. R., & Djorgovski, S. G. 2002, AJ, 123, 1111
Bruzual, G., & Charlot, S. 2003, MNRAS, 344, 1000
Burrows, D. N., Grupe, D., Capalbi, M., et al. 2006, ApJ, 653, 468
Burrows, D. N., Hill, J. E., Nousek, J. A., et al. 2005, SSRv, 120, 165
Cannizzo, J. K., Troja, E., & Gehrels, N. 2011, ApJ, 734, 35
Cenko, S. B., Frail, D. A., Harrison, F. A., et al. 2010, ApJ, 711, 641
Cepa, J., Bland-Hawthorn, J., González, J. J. & OSIRIS Consortium 2000, in ASP Conf. Ser. 195, Imaging the Universe in Three Dimensions, ed. W. van Breugel & J. Bland-Hawthorn, (San Francisco, CA: ASP), 597
Chabrier, G. 2003, PASP, 115, 763
Cordes, J. M., & Lazio, T. J. W. 2002, arXiv:astro-ph/0207156
Corsi, A., Guetta, D., & Piro, L. 2010, ApJ, 720, 1008
Coward, D. M., Howell, E. J., Piran, T., et al. 2012, MNRAS, 425, 2668
Cummings, J. R., Burrows, D. N., Evans, P. A., et al. 2014, GCN, 16763, 1
D'Avanzo, P., Malesani, D., Covino, S., et al. 2009, A&A, 498, 711
D'Avanzo, P., Salvaterra, R., Bernardini, M. G., et al. 2014, MNRAS, 442, 2342
De Pasquale, M., Schady, P., Kuin, N. P. M., et al. 2010, ApJL, 709, L146
Duffell, P. C., Quataert, E., & MacFadyen, A. I. 2015, ApJ, 813, 64
Fan, Y.-Z., & Wei, D.-M. 2011, ApJ, 739, 47
Fan, Y.-Z., & Xu, D. 2006, MNRAS, 372, L19
Ferrero, P., Kann, D. A., Zeh, A., et al. 2006, A&A, 457, 857

Fong, W., Berger, E., Margutti, R., et al. 2012, ApJ, 756, 189
Fong, W., Berger, E., Margutti, R., & Zauderer, B. A. 2015, ApJ, 815, 102
Foucart, F., Deaton, M. B., Duez, M. D., et al. 2014, PhRvD, 90, 024026
Galama, T. J., Vreeswijk, P. M., van Paradijs, J., et al. 1998, Natur, 395, 670
Gao, H., Ding, X., Wu, X.-F., Dai, Z.-G., & Zhang, B. 2015, ApJ, 807, 163
Gehrels, N., Norris, J. P., Barthelmy, S. D., et al. 2006, Natur, 444, 1044
Gehrels, N., Sarazin, C. L., O'Brien, P. T., et al. 2005, Natur, 437, 851
Giacomazzo, B., & Perna, R. 2013, ApJL, 771, L26
Giacomazzo, B., Perna, R., Rezzolla, L., Troja, E., & Lazzati, D. 2013, ApJL, 762, L18
Hook, I. M., Jørgensen, I., Allington-Smith, J. R., et al. 2004, PASP, 116, 425
Ilbert, O., Arnouts, S., McCracken, H. J., et al. 2006, A&A, 457, 841
Janka, H.-T., Aloy, M.-A., Mazzali, P. A., & Pian, E. 2006, ApJ, 645, 1305
Jin, Z.-P., Hotokezaka, K., Li, X., et al. 2016, arXiv:1603.07869
Jin, Z.-P., Li, X., Cano, Z., et al. 2015, ApJL, 811, L22
Kalberla, P. M. W., Burton, W. B., Hartmann, D., et al. 2005, A&A, 440, 775
Kann, D. A., Klose, S., Zhang, B., et al. 2011, ApJ, 734, 96
Kasen, D., Fernández, R., & Metzger, B. D. 2015, MNRAS, 450, 1777
Kennicutt, R. C., Jr. 1998, ARA&A, 36, 189
Kouveliotou, C., Meegan, C. A., Fishman, G. J., et al. 1993, ApJL, 413, L101
Kraft, R. P., Burrows, D. N., & Nousek, J. A. 1991, ApJ, 374, 344
Levesque, E. M., Bloom, J. S., Butler, N. R., et al. 2010, MNRAS, 401, 963
Li, L.-X., & Paczyński, B. 1998, ApJL, 507, L59
Lippuner, J., & Roberts, L. F. 2015, ApJ, 815, 82
Lyons, N., O'Brien, P. T., Zhang, B., et al. 2010, MNRAS, 402, 705
Mészáros, P., & Rees, M. J. 1997, ApJ, 476, 232
Metzger, B. D., Martínez-Pinedo, G., Darbha, S., et al. 2010, MNRAS, 408, 2650
Nagakura, H., Hotokezaka, K., Sekiguchi, Y., Shibata, M., & Ioka, K. 2014, ApJL, 784, L28
Nagao, T., Maiolino, R., & Marconi, A. 2006, A&A, 459, 85
Nicuesa Guelbenzu, A., Klose, S., Krühler, T., et al. 2012, A&A, 538, L7
Norris, J. P., & Bonnell, J. T. 2006, ApJ, 643, 266
Perley, D. A., Modjaz, M., Morgan, A. N., et al. 2012, ApJ, 758, 122
Perna, R., Lazzati, D., & Giacomazzo, B. 2016, ApJL, 821, L18
Rezzolla, L., Giacomazzo, B., Baiotti, L., et al. 2011, ApJL, 732, L6
Planck Collaboration, Ade, P. A. R., Aghanim, N., et al. 2015, arXiv:1502.01589
Rhoads, J. E. 1999, ApJ, 525, 737
Rowlinson, A., O'Brien, P. T., Metzger, B. D., Tanvir, N. R., & Levan, A. J. 2013, MNRAS, 430, 1061
Ruffert, M., & Janka, H.-T. 1999, A&A, 344, 573
Sakamoto, T., Sato, G., Barbier, L., et al. 2009, ApJ, 693, 922
Sari, R., Piran, T., & Halpern, J. P. 1999, ApJL, 519, L17
Savaglio, S., Glazebrook, K., & Le Borgne, D. 2009, ApJ, 691, 182
Schlegel, D. J., Finkbeiner, D. P., & Davis, M. 1998, ApJ, 500, 525
Serino, M., Sakamoto, T., Kawai, N., et al. 2014, GCN, 16778, 1
Setiawan, S., Ruffert, M., & Janka, H.-T. 2004, MNRAS, 352, 753
Shapiro, S. L., & Teukolsky, S. A. 1983, Black Holes, White Dwarfs, and Neutron Stars: The Physics of Compact Objects (Hoboken, NJ: Wiley)
Skrutskie, M. F., Cutri, R. M., Stiening, R., et al. 2006, AJ, 131, 1163
Stratta, G., D'Avanzo, P., Piranomonte, S., et al. 2007, A&A, 474, 827
Tanvir, N. R., Levan, A. J., Fruchter, A. S., et al. 2013, Natur, 500, 547
Thöne, C. C., Campana, S., Lazzati, D., et al. 2011, MNRAS, 414, 479
Thorne, K. S. 1987, Gravitational Radiation, ed. S. W. Hawking & W. Israel (Cambridge: Cambridge Univ. Press)
Tody, D. 1993, in ASP Conf. Ser. 52, Astronomical Data Analysis Software and Systems II, ed. R. J. Hanisch, R. J. V. Brissenden, & J. Barnes 173
Troja, E., Cusumano, G., O'Brien, P. T., et al. 2007, ApJ, 665, 599
Troja, E., King, A. R., O'Brien, P. T., Lyons, N., & Cusumano, G. 2008, MNRAS, 385, L10
Troja, E., Read, A. M., Tiengo, A., & Salvaterra, R. 2016, ApJL, 822, L8
Ukwatta, T. N., Dhuga, K. S., Stamatikos, M., et al. 2012, MNRAS, 419, 614
van Eerten, H. 2014, MNRAS, 442, 3495
van Eerten, H., & MacFadyen, A. 2013, ApJ, 767, 141
van Eerten, H., Zhang, W., & MacFadyen, A. 2010, ApJ, 722, 235
Virgili, F. J., Zhang, B., O'Brien, P., & Troja, E. 2011, ApJ, 727, 109
Willingale, R., Starling, R. L. C., Beardmore, A. P., Tanvir, N. R., & O'Brien, P. T. 2013, MNRAS, 431, 394
Willmer, C. N. A., Faber, S. M., Koo, D. C., et al. 2006, ApJ, 647, 853
Yang, B., Jin, Z.-P., Li, X., et al. 2015, NatCo, 6, 7323
Yasuda, N., Fukugita, M., Narayanan, V. K., et al. 2001, AJ, 122, 1104
Yu, Y.-W., Zhang, B., & Gao, H. 2013, ApJL, 776, L40
Zhang, B., Fan, Y. Z., Dyks, J., et al. 2006, ApJ, 642, 354
Zhang, B., & Mészáros, P. 2001, ApJL, 552, L35
Zhang, B., & Mészáros, P. 2004, IJMPA, 19, 2385
Zhang, B.-B., van Eerten, H., Burrows, D. N., et al. 2015, ApJ, 806, 15